Equilibrium Behavior of a Tethered Autogyro: Application in Extended Flight and Power Generation

Jonathan McConnell

Mechanical and Aerospace Engineering, University of Central Florida, Orlando, FL 32816 e-mail: Jonathan.McConnell@knights.ucf.edu

Tuhin Das¹

Associate Professor Mechanical and Aerospace Engineering, University of Central Florida, Orlando, FL 32816 e-mail: Tuhin.Das@ucf.edu

In this article, we study the characteristics of steady autorotation of a tethered autogyro. The phenomenon of autorotation refers to the natural spinning of a rotor in a wind field. We explore the viability of tethered autogyros as unmanned aerial vehicles (UAVs) for long-duration and energy efficient hovering applications, such as in monitoring or surveillance. The tether provides mooring and can be used to power the rotor and to transmit wind power to the ground when suitable. This is a novel application of autorotation. It requires a generalized formulation and modeling of autorotation, beyond what is reported in the literature. We adopt a model-based approach where the blade element momentum (BEM) method and catenary mechanics are used to model the aerodynamics and the tether, respectively. The resulting model is highly nonlinear and numerical methods are proposed to solve for the equilibria. The model is validated against existing simulation and experimental results in the literature. It is extended to incorporate new features that are pertinent to our application, such as low rotor speeds, regenerative torque for power generation, combining catenary mechanics with aerodynamics, and varying atmospheric conditions with altitude. We characterize the autorotational equilibria over a range of operating conditions involving multiple independent variables. The analysis reveals an optimal operating range of the tip speed ratio of the autogyro under equilibrium. It also indicates the possibility of power generation in large autogyros stationed at high altitudes. [DOI: 10.1115/1.4054927]

Keywords: aerodynamics, dynamics

1 Introduction

An unpowered rotorcraft producing steady lift from self-rotating blades is in a state of autorotation. Harnessing significant prevailing winds found consistently at high altitudes [1–5], and it is possible for an autorotating rotorcraft, or autogyro, to generate power. This ability can be exploited for the purpose of extended, efficient flight of rotorcraft, and can provide a platform for accessing the largely untapped energy source of high-altitude jet streams. This document presents a numerical model for describing a tethered, power-generating autogyro and analyzes the feasible flight region to verify practicality for both a larger, high-altitude configuration focusing on power generation, and a smaller, lower altitude configuration focused on energy efficient flight for surveillance applications.

Many efforts have been made to explore the power generation capabilities of airborne wind energy (AWE) systems in the form of tethered airfoils/kites, [6–14], as well as lighter-than-air (LTA) tethered wind turbines [15–17]. Airfoil/kite AWEs largely rely on mechanical stimulation of the tether through crosswind maneuvers. Thus, such a system becomes impractical at higher altitudes where wind energy density is prominent, as increased uncertainty in tether dynamics can decrease the efficiency of mechanical transmission to the base. LTA windmills may be effective at higher altitudes, but are quite lacking in maneuverability, as suggested by Ref. [18], which can be essential for effective surveillance. The use of tethered autorotation combines the benefits of on-board power generation

seen in LTAs with the heightened maneuverability of smaller, and more aerodynamic designs are seen in airfoil/kite AWEs.

A review of the timeline and challenges of autogyro development is presented in Refs. [19,20]. Following the creation of autogyros for piloted flight in the early 1920s, Glauert [21] developed a compact initial model for describing the steady-state behavior of an autogyro utilizing the blade element momentum approach [22]. Many works followed to relax the assumptions of Ref. [21] and expand upon their model [23-27]; perhaps most notable of which is the work of Wheatley [25], who not only presented a more detailed model but also provided experimental validation through testing on a commercially available autogyro of the time. This analysis expanded upon Ref. [21] to include a linear variation in pitch. Further work in Ref. [28] expanded the analysis to explore the effects of periodic blade twist. Many works have focused on autorotation in the context of the descent of a helicopter [29]. Analysis of autogyro performance analogous to the flight modes of helicopters and fixed-wing vehicles is also present in the literature [30], with some works testing and modeling the performance of hybrid rotor/fixed-wing crafts in the conditions of autorotation [31–33]. In Ref. [34,35], a simple model was tuned through small-scale experimentation to explore instability in autorotation. In this article, we take a different approach considering the context of a stationary tethered rotorcraft autorotating in a prevailing wind field. It is unpowered when autorotating, and if excess wind power is available at its operating altitude, it can transfer the power to ground via

Improving upon Ref. [25], initial efforts have been made in Refs. [36–39] to model and explore the effects of regenerative braking on the steady-state behavior of an autogyro, as well as the practicality of tethered autorotation as a source of high-altitude power generation. The following document provides an updated and refined numerical method for solving aerodynamic equilibrium

¹Corresponding author.

Contributed by the Applied Mechanics Division of ASME for publication in the JOURNAL OF APPLIED MECHANICS. Manuscript received December 13, 2021; final manuscript received May 18, 2022; published online July 19, 2022. Assoc. Editor: Ahmet S. Yigit.

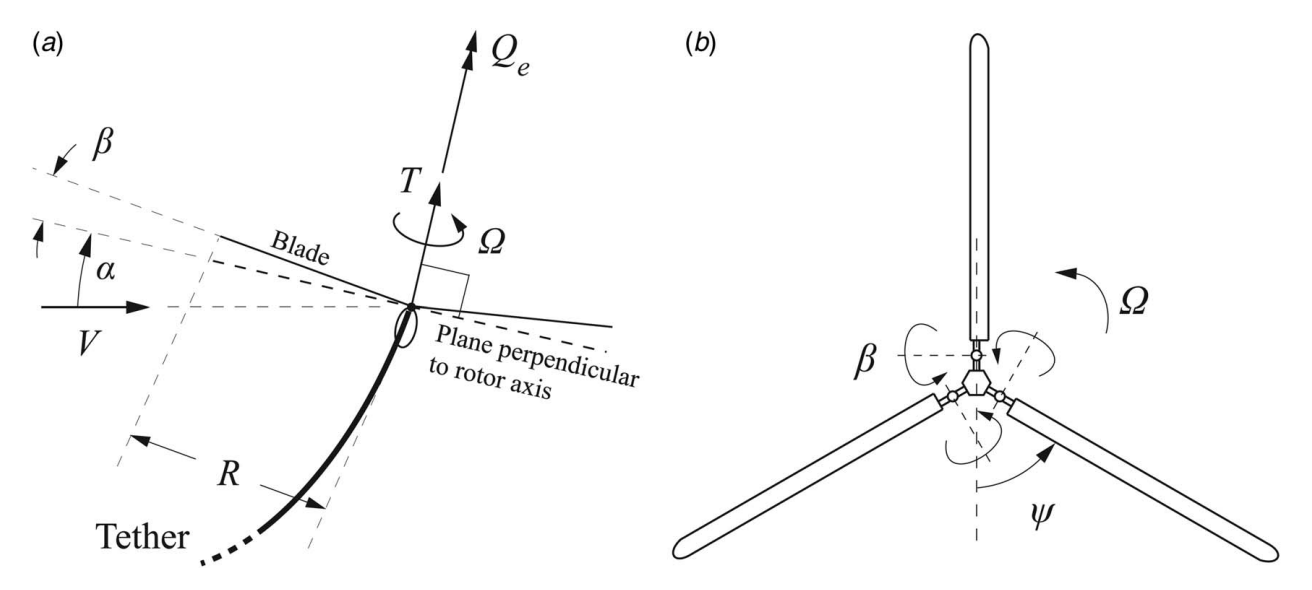


Fig. 1 (a) Side view of tethered autogyro and (b) top view of hinged autogyro blades

behavior. An additional numerical method is presented to couple the response of a static tether to the aerodynamic forces provided by an autogyro in a realistic wind profile. The coupled numerical process has been thoroughly simulated to visualize the steady-state behavior of a tethered autogyro over a dense range of inputs, not only for the case of high-altitude power generation but also lower altitude surveillance. The contributions of this work are as follows:

- The aerodynamics of autorotation is generalized by incorporating regenerative braking, lower rotor speeds, and wind velocity and atmospheric density variations with altitude.
- Numerical methods are proposed to solve for the equilibrium conditions.
- (3) The generalizations yield a larger space of equilibrium conditions of the system.
- (4) Tether mechanics are incorporated and equilibria are determined for the tether-autogyro assembly.
- (5) The possibility of power generation is quantitatively explored through this model-based approach.

The rest of this article is organized as follows: In Sec. 2, we present the aerodynamic model that incorporates regenerative braking and lower rotor speeds. A numerical approach to solve for equilibrium conditions and model validation results is provided. Section 3 presents the model of the catenary. In Sec. 4, we discuss the numerical approach to solve for the equilibria of the combined tether-autogyro system in the presence of wind speeds and air density, which vary with altitude. Simulation results are provided in Sec. 5. This is followed by concluding remarks, acknowledgments, and references.

2 Autorotational Equilibria: Incorporating Regenerative Braking and Low Rotor Speeds

2.1 Aerodynamic Model. The model presented here expands upon the work of Wheatley, [25], to explore the equilibrium aerodynamic behavior of an autogyro under regenerative braking and low rotor speeds. With this as the focus, we skip the details of model development, for which the reader is suggested to read [25,36]. Here, we concisely present the governing equations for steady autorotation. Consider a tethered autogyro under equilibrium conditions, as shown in Fig. 1(a). In describing the aerodynamics, this model employs the use of two dimensionless ratios shown in Eq. (1).

$$\mu = \frac{V \cos \alpha}{\Omega R}, \quad \lambda = \frac{V \sin \alpha - v}{\Omega R}$$
 (1)

The variables V, α , ν , and Ω and the parameter R are defined in the nomenclature. The variable μ , the tip speed ratio, is the ratio of the component of the wind velocity parallel to the rotor disc to the speed of the tip of the rotor blade. The variable λ , the axial flow ratio, is the ratio of the total flow perpendicular to the rotor disc to the speed of the tip. Rotor blades of an autogyro are hinged at the base allowing a flapping motion, which naturally balances the rolling torque of the craft. A visualization of the hinge mechanism is shown in Fig. 1(b). This flapping dynamic of a blade can be approximated by a periodic function of its angular position ψ , as a truncated Fourier series containing five coefficients, as shown in Eq. (2).

$$\beta = a_0 - a_1 \cos \psi - b_1 \sin \psi - a_2 \cos 2\psi - b_2 \sin 2\psi \tag{2}$$

where β is the flapping angle of a blade (see Fig. 1(b)). The values a_0 , a_1 , b_1 , a_2 , and b_2 are the coefficients of the Fourier series. It has been shown in Ref. [25] that these coefficients can be written as a function of μ and λ , as given in Eqs. (3)–(7).

$$a_0 = \frac{1}{2} \gamma \left\{ \frac{1}{3} \lambda B^3 + 0.080 \mu^3 \lambda + \frac{1}{4} \theta_0 \left(B^4 + \mu^2 B^2 - \frac{1}{8} \mu^4 \right) + \frac{1}{5} \theta_1 \left(B^5 + \frac{5}{6} \mu^2 B^3 \right) + \frac{1}{8} \mu^2 b_2 B^2 \right\} - \frac{M_W}{I_1 \Omega^2}$$
(3)

 $a_{1} = \frac{2\mu}{B^{4} - \frac{1}{2}\mu^{2}B^{2}} \left\{ \lambda \left(B^{2} - \frac{1}{4}\mu^{2} \right) + \frac{4}{3}\theta_{0}B^{3} + 0.106\mu^{3}\theta_{0} + \theta_{1}B^{4} - \frac{1}{3}b_{2}B^{3} \right\}$ (4)

$$b_1 = \frac{4\mu B}{B^2 + \frac{1}{2}\mu^2} \left\{ \frac{1}{3}a_0 + \frac{0.035}{B^3}\mu^3 a_0 + \frac{1}{6}a_2 \right\}$$
 (5)

$$3a_2 - \frac{1}{4}\gamma b_2 B^4$$

$$= \frac{1}{2}\gamma \mu^2 \left\{ -\frac{1}{4}\theta_0 \left(B^2 - \frac{1}{8}\mu^2 \right) - \frac{1}{6}\theta_1 B^3 - 0.053\mu\lambda + \frac{1}{3}\frac{a_1}{\mu} B^3 \right\}$$
(6)

$$3b_2 + \frac{1}{4}\gamma a_2 B^4 = \frac{1}{2}\gamma \mu^2 \left\{ -\frac{1}{4}a_0 \left(B^2 - \frac{1}{6}\mu^2 \right) + \frac{1}{3}\frac{b_1}{\mu} B^3 \right\}$$
 (7)

where γ , B, θ_0 , and θ_1 are defined in the Nomenclature and blade pitch θ is considered to vary along the radial distance r according to, $\theta = \theta_0 + (r/R)\theta_1$. The nondimensional mass constant γ is given by

$$\gamma = \frac{c\rho a R^4}{I_1} \tag{8}$$

where c, ρ , a, R, and I_1 are defined in the Nomenclature. It is noted that Eqs. (3)–(7) are derived using Eq. (2) and the flapping dynamics of each blade, given by

$$I_1 \left(\frac{d^2 \beta}{dt^2} + \Omega^2 \beta \right) = M_T - M_W \tag{9}$$

where β , Ω , M_T , and M_W are defined in the Nomenclature. The term $M_W/I_1\Omega^2$ in Eq. (3) is considered negligible in Ref. [25]. This is because Wheatley [25] considers autorotation in the context of a powered rotor, such as a helicopter, where Ω is much higher compared to a rotor freely autorotating under different ambient wind speeds. Since we consider the latter scenario, this assumption must be removed. However, removing this assumption requires a considerable complication in how the autorotational equilibria are calculated. The consequence of relaxing this assumption will be clear in validation results, to be presented in Sec. 2.2.

For an autogyro undergoing steady autorotation, the aerodynamic torque about the rotor will be equal to that of the applied regenerative braking, Q_e . The introduction of regenerative braking in the aerodynamics is critical to this study since our goal is to explore the potential of such tethered autogyros to not only be stationed at a certain location but also produce energy from the ambient wind field, when possible. The torque balance can be rearranged to yield an expression shown in Eq. (10).

$$\begin{split} \frac{2Q_e}{b\rho c\Omega^2 R^4 a} &= \lambda^2 \left(\frac{1}{2}B^2 - \frac{1}{4}\mu^2\right) \\ &+ \lambda \left(\frac{1}{3}\theta_0 B^3 + \frac{2}{9\pi}\mu^3 \theta_0 + \frac{1}{4}\theta_1 B^4 + \frac{1}{32}\mu^4 \theta_1\right) \\ &+ \mu \lambda a_1 \left(\frac{1}{2}B^2 - \frac{3}{8}\mu^2\right) + a_0^2 \left(\frac{1}{4}\mu^2 B^2 - \frac{1}{16}\mu^4\right) \\ &- \frac{1}{3}\mu a_0 b_1 B^3 + a_1^2 \left(\frac{1}{8}B^4 + \frac{3}{16}\mu^2 B^2\right) \\ &+ b_1^2 \left(\frac{1}{8}B^4 + \frac{1}{16}\mu^2 B^2\right) - a_2 \left(\frac{1}{4}\mu^2 a_0 B^2 + \frac{1}{6}\mu b_1 B^3\right) \\ &+ \frac{1}{2}a_2^2 B^4 + b_2 \left(\frac{1}{8}\mu^2 \theta_0 B^2 + \frac{1}{12}\mu^2 \theta_1 B^3 + \frac{1}{6}\mu a_1 B^3\right) \\ &+ \frac{1}{2}b_2^2 B^4 - \frac{\delta}{4a} \left(1 + \mu^2 - \frac{1}{8}\mu^4\right) \end{split} \tag{10}$$

The parameters b, c, a, and δ are defined in the nomenclature. The introduction of the regenerative braking torque Q_e is another major departure from Wheatley [25], where the left-hand side of Eq. (10) is set to zero as no regenerative braking is applied. In that case, a value of λ could be solve for irrespective of Ω and Q_e . In the presented model, an input value is selected for Q_e , but Ω and λ must be solved simultaneously. Solving for λ allows for the coefficient of thrust C_T to be expressed as a function of μ , given by

$$C_{T} = \frac{T}{\rho \Omega^{2} \pi R^{4}} = \frac{1}{2} \sigma a \left[\frac{1}{2} \lambda \left(B^{2} + \frac{1}{2} \mu^{2} \right) + \theta_{0} \left(\frac{1}{3} B^{3} + \frac{1}{2} \mu^{2} B - \frac{4}{9 \pi} \mu^{3} \right) + \theta_{1} \left(\frac{1}{4} B^{4} + \frac{1}{4} \mu^{2} B^{2} - \frac{1}{32} \mu^{4} \right) + \frac{1}{4} \mu^{2} b_{2} B + \frac{1}{8} \mu^{3} a_{1} \right]$$

$$(11)$$

where *T* is the thrust and σ is the solidity of the blade disc. The angle of incidence α , Fig. 1(a), is given by

$$\tan \alpha = \frac{\lambda}{\mu} + \frac{\frac{1}{2}C_T}{\mu(\lambda^2 + \mu^2)^{1/2}}$$
 (12)

Realistically, the induced velocity is not uniform across the rotor disc. This variation can be approximated by the sinusoidal variation given in Eq. (13) [25].

$$v_1 = Kv \frac{r}{R} \cos \psi \tag{13}$$

where K is the amplitude of flow variation. Applying this velocity variation produces a correction term for λ in the form of Eq. (14) [25].

$$\lambda_1 = \frac{\frac{1}{2}KC_T}{(\mu^2 + \lambda^2)^{1/2}} \tag{14}$$

The influence of the variable flow requires an update to the values of the flapping coefficients, which can be seen in Eq. (15). Furthermore, the terms of Eq. (16) must be appended to Eq. (10) so that an updated value of λ can be retrieved.

$$\Delta b_1 = \frac{\lambda_1 B^2}{B^2 + \frac{1}{2}\mu^2}; \quad \Delta a_2 = \frac{-\frac{1}{3}\mu\gamma^2\lambda_1 B^7}{144 + \gamma^2 B^8}; \quad \Delta b_2 = \frac{-4\mu\gamma\lambda_1 B^3}{144 + \gamma^2 B^8}$$

$$\frac{1}{8}\lambda_1^2 B^4 + \frac{1}{3}\mu\lambda_1 a_0 B^3 - \frac{1}{4}\lambda_1 b_1 B^4 - \frac{1}{6}\mu\lambda_1 a_2 B^3 - \frac{8}{45\pi}a_0\lambda_1 \mu^4 - \frac{1}{64}\lambda_1^2 \mu^4$$
(16)

In Wheatley's work, [25], the exclusion of the final term in Eq. (3) allows for a complete description of autogyro aerodynamics with only one input of μ . This description is compact and can be solved analytically, but is limited to a one-dimensional equilibrium space associated with a particular relation between wing load and μ . Inclusion of the final term in Eq. (3) and implementation of a numerical method produces Ω as an output. While this complicates the process for solving the aerodynamic steady-state behavior, it also expands the equilibrium space to include the ambient wind speed. Further, with the inclusion of regenerative braking Q_e , the presented model explores a wider three-dimensional input space and thus is representative of the behavior for a much larger set of equilibrium conditions of an autogyro.

2.1.1 Numerical Solution of Equilibria. In this section, we present an algorithm that can be used to determine the various autorotational equilibria. The proposed algorithm considers three variables, namely μ , Q_e , and V, to form the input space of the autorotational equilibria. A total of ten unknown variables are determined from the set of nonlinear equations composed of Eqs. (1)–(12) and Eq. (14) (with the adjustments of Eqs. (15) and (16)). Due to the coupling of equations introduced by the inclusion of the final term in Eq. (3) and the addition of regenerative braking in Eq. (10), an iterative solving method is necessary to converge on an equilibrium state. A suggested numerical process is presented below:

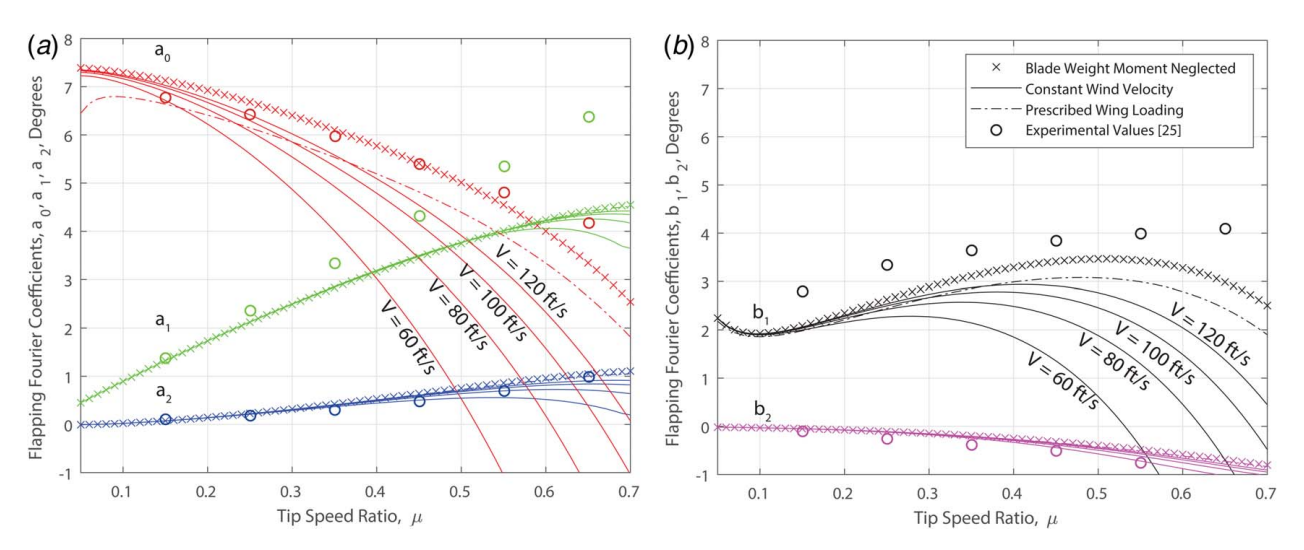


Fig. 2 Flapping coefficient behavior for various wind velocity inputs: (a) a0, a1, a2 and (b) b1, b2

- (1) Provide a selected μ , Q_e , and V.
- (2) Initialize λ and α with reasonable guesses.
- (3) Calculate Ω with the tip speed relation of Eq. (1).
- (4) Calculate a_0 , a_1 , b_1 , a_2 , and b_2 with Eqs. (3)–(7).
- (5) Calculate λ with Eq. (10).
- (6) Calculate C_T with Eq. (11).
- (7) Calculate λ_1 with Eq. (14).
- (8) Adjust b_1 , a_2 , and b_2 with Eq. (15).
- (9) Recalculate λ by appending Eq. (16) to Eq. (10).
- (10) Calculate α with Eq. (12).
- (11) Adjust guesses for λ and α in direction of calculated values.
- (12) Repeat steps 3–11 until the absolute change of λ and α is below a desired threshold suggesting convergence (chosen as 10^{-5} in this study).

2.2 Model Validation. In the development of the presented model, the assumption of a nonnegligible effect of the blade weight moment term in Eq. (3) was relaxed, and a regenerative braking torque, Q_e , was incorporated to increase the input space to that of three inputs, namely, μ , Q_e , and V. This provides a broader insight into the possible equilibrium space for autorotation than that of Wheatley [25]. It follows that, for validation against the experimental results provided in Ref. [25], special attention must be given to selecting an appropriate contour of inputs for direct comparison with the experimental data. The comparison data was done by prescribing a wing load for each value of μ considered. This wing load was used to calculate the rotor speed. A side effect of this prescribed wing loading profile is that V is not uniform across the span of μ . Thus, it is necessary, for comparison of the presented model and experimental results, to input experimental values of μ , Ω , and α into Eq. (1) to retrieve an analogous value for V, which can be used as input to the presented model for each value of μ . It should be noted that, for validation against experimental data, Q_e must be set to zero as it [25] does not consider regenerative braking. Further, the values of parameters must also be consistent. In this regard, the following table gives a list of parameter values used for the model,

$$a = 5.85$$
 $b = 4$ $B = 0.9593$ $c = 1.833 ft$ $I_1 = 334 \frac{slug}{f^2}$ $K = 0.5$ $m_a = 23.3 slug$ $M_W = 715.799 ft lb$ $R = 22.5 ft$ (17) $\gamma = 17.2791$ $\delta = 0.012$ $\theta_0 = 0.0384$ $\theta_1 = 0.0001256$ $\sigma = 0.1037$

Figure 2 displays simulated profiles for the flapping Fourier coefficients of Eq. (2). The trends denoted by x's represent the presented model with the blade weight moment term of Eq. (3) neglected. The

profiles resulting from this assumption are independent of wind velocity, V. With the blade weight moment term of Eq. (3) included in the analysis, consideration of V becomes important. This is apparent by observing the solid contours representing constant V across the span of μ . The dash-dot profile is the simulated results with the blade weight moment term of Eq. (3) incorporated while selecting input V values analogous to that of the experimental data, as outlined in the previous paragraph. The experimental data collected by Wheatley [25] is visualized with circular points. As the assumption of a nonnegligible effect of blade weight moment directly pertains to Eq. (3), it is reasonable that a_0 would be the most significantly affected coefficient. The other four coefficients are negligibly affected by the inclusion of the blade weight moment term of Eq. (3), especially in the region μ <0.5. It was suggested by Glauert [21] and substantiated by experiments in Ref. [25] that μ < 0.5 is the range of validity for blade element momentum calculations. This is based on the condition that the relative wind velocity be positive over the outer half of the retreating blade. Thus, it is expected that error will occur beyond this point. The adjusted magnitude of a_0 directly relates to the average of the flapping angle, β . It can be observed that for high wind velocities, V, the assumption of a negligible effect of blade weight moment becomes more and more accurate. It follows from Eq. (1) that, for a given μ and uniform α , a larger V will result in higher angular velocity Ω . Therefore, by providing sufficiently large V and sustaining a nonzero value of $\cos \alpha$, the final term of Eq. (3) will be dominated by its denominator and thus be rendered negligible.

In Figs. 2-4, note the trends labeled "Prescribed Wing Loading." These trends are obtained under the specific flight conditions used to report results in the study by Wheatley [25]. We include these specific trends to put our results in context. The wing loading refers to the weight per unit area supported by the fixed wing of the PCA-2 Autogyro, whose experimental results are reported in Ref. [25]. The PCA-2 Autogyro has both a fixed wing and a rotor. The experimental setup and data are detailed in Ref. [31]. The prescribed wing loading has a specific one-to-one correspondence with the air-speed of the PCA-2 Autogyro, which is equivalent to the wind velocity, V, in our work. It also has a similar dependence with the tip-speed ratio μ of the rotor. Thus, the data in Ref. [31] effectively considers V as a function of μ . In Ref. [25], this relationship is not explicitly given. However, it can be determined from the Ω versus μ and α versus μ data, together with the definition of μ . The calculated dependence matches closely with the experimentally obtained relation reported in Ref. [31]. For example, from Ref. [31], the wing aloading at $\mu =$ 0.25 is $\approx 20\%$, which corresponds to an effective air speed of \approx 56 mph (equivalent to \approx 82 ft/s). It can be observed in Fig. 4

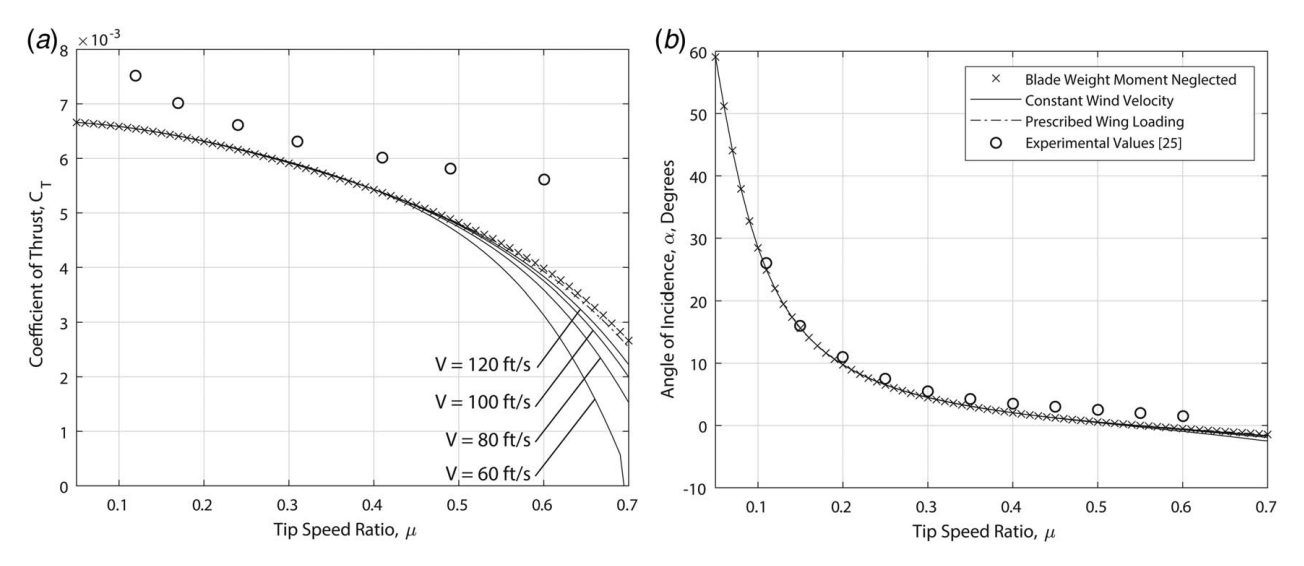


Fig. 3 (a) Coefficient of thrust and (b) Angle of incidence for various wind velocity inputs. Note: Trends identified in legend are almost coincident in (b) but show diversion in (a) at high μ values.

that the "Prescribed Wing Loading" trend as well as the data cross the velocity level curves at ≈ 82 ft/s.

In Fig. 3, it can be seen that the coefficient of thrust C_T is largely independent of V below $\mu = 0.5$, where as angle of incidence, α , displays only negligible changes with respect to V for the entire range of μ . While the model results show deviation from the experimental data of C_T , this deviation is particularly small (within $\approx 5\%$) in the range $0.15 < \mu < 0.35$, a region where feasible autorotational equilibria are predominantly concentrated. It is noted that for $\mu < 0.1$, α assumes large angles where the momentum theory is not valid and hence model predictions for $\mu < 0.1$ may not be reliable. The angular velocity Ω shown in Fig. 4 varies significantly with differing V. It can be seen from the dash-dot line in Fig. 4 that the prescribed-wing-loading-based V generates nearly constant Ω over the range $\mu > 0.1$. This behavior as well as the magnitude

agrees with the experimental behavior over the range of $0.1 < \mu < 0.5$ reported by Wheatley [25]. The trends of Fig. 4 are representative of a nonnegligible effect of blade weight moment, but it was observed that exclusion of this term does not significantly affect the value of Ω . Comparison to the results of Ref. [25] was shown for a case of no regenerative braking, i.e., for $Q_e = 0$.

Addition of regenerative braking significantly affects the performance of an autogyro, and thus, the visuals presented in Figs. 5–7 serve to provide insight into this behavior. The solid trends represent a constant input of torque with consideration to nonnegligible blade weigh moment effects; the dash-dot trends show the same torque applied with blade weight moment neglected. These trends were simulated at a constant wind velocity of 100 ft/s. The behavior of a_0 , a_1 , a_2 , b_1 , and b_2 with differing torque input is displayed in Fig. 5. The increase in magnitude with increasing torque

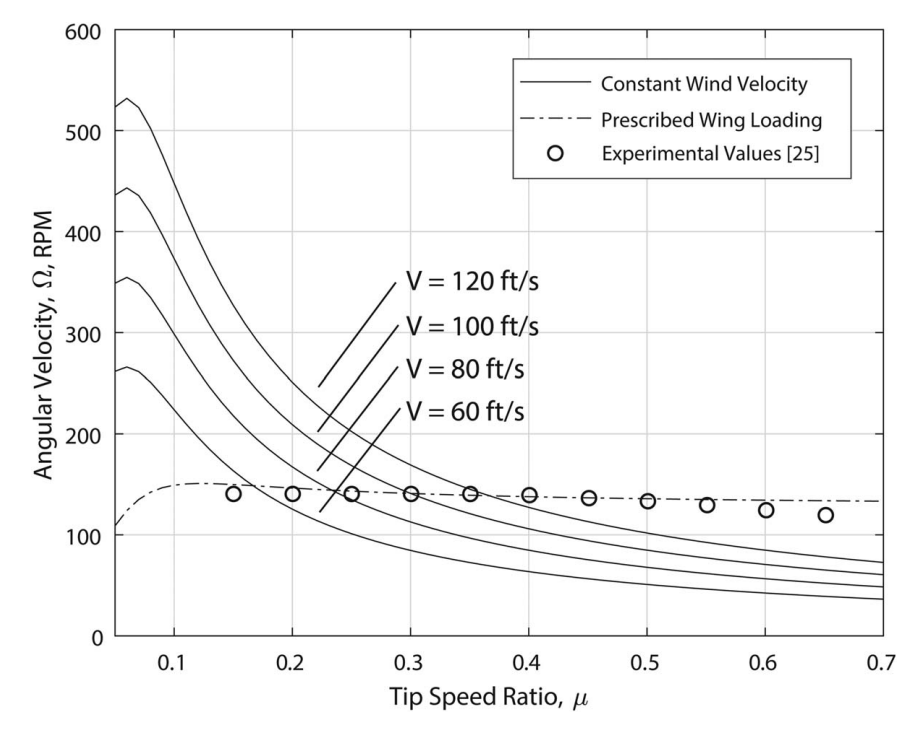


Fig. 4 Angular velocity for various wind velocity inputs

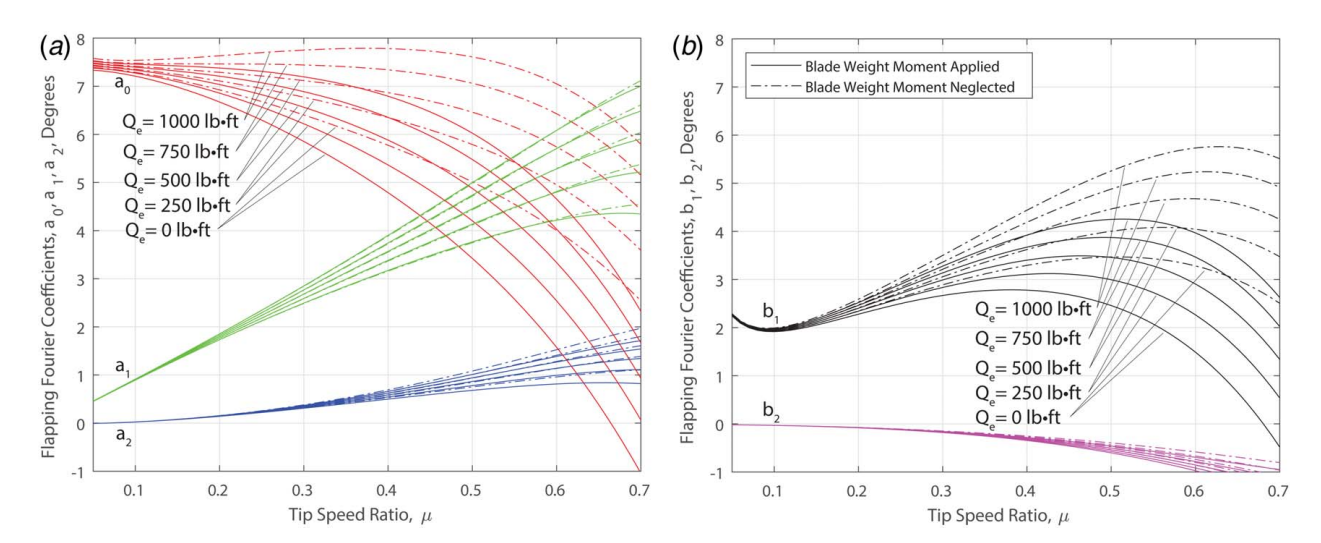


Fig. 5 Flapping coefficient for various torque inputs at V = 100 ft/s: (a) a_0 , a_1 , a_2 and (b) b_1 , b_2

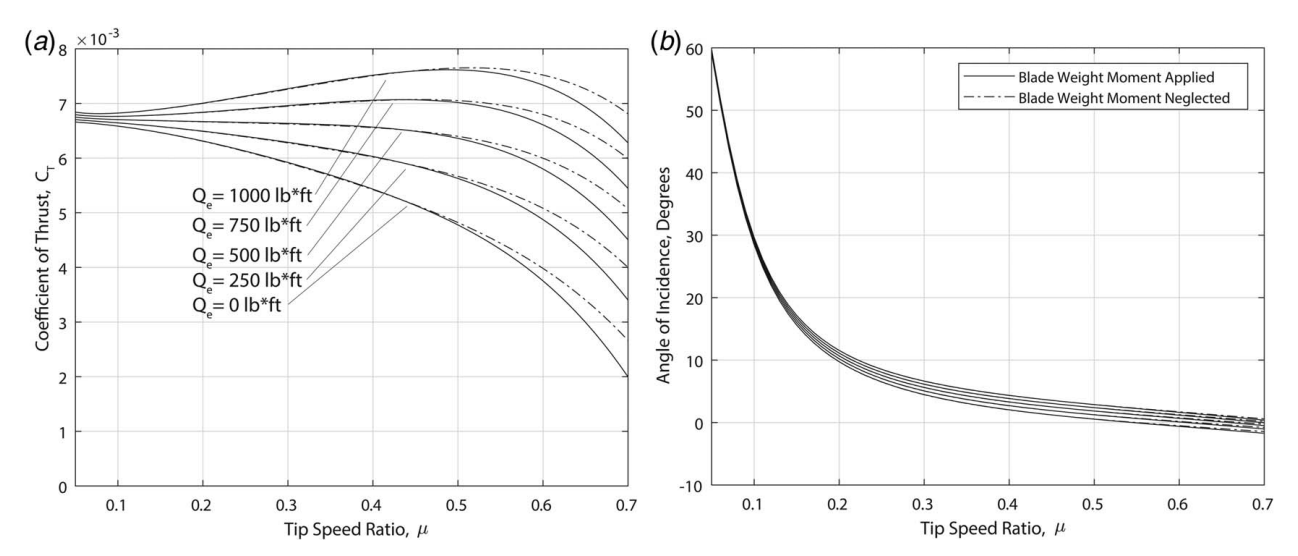


Fig. 6 (a) Coefficient of thrust and (b) angle of incidence for various torque inputs at V = 100 ft/s. Note: Trends identified in legend are almost overlapping in (b) and hence indiscernible.

relationship seen for a_0 and b_1 is also true for the remaining coefficients, and thus, the same constant torque inputs from 0 to 1000 lb· ft should be associated with the a_1 , a_2 , and b_2 trends from bottom to top, respectively. This increase in flapping coefficient magnitude suggests an overall increase to the average flapping angle as well as the variation of the flapping angle over a full rotation of the rotor. A similar trend is shown in Fig. 6(a) with regards to the coefficient of thrust, C_T . Once again, C_T does not appear to be significantly affected by the inclusion of the effects of the blade weight moment term of Eq. (3); however, an increase in regenerative braking does appear to change the performance, suggesting the ability to tune the thrust output of an autogyro with regenerative braking. The parameters α and Ω remain largely unaffected by a change in input torque.

It should be noted that the plots shown are in relation to a span of μ . The ratio μ is defined in Eq. (1) to be a function of V, α , and Ω . With μ and V being inputs, it follows from this observation that the weak relationship between Q_e and α causes only a small change in Ω with different input Q_e . Logic and experience tells us that applying a braking torque to a rotating shaft will decrease its angular speed; however, by selecting a value for μ as input, the presented model neglects causality. As this work is an exploration of

steady-state behavior, it need not be upheld to the same causal demands of dynamic analysis. Nevertheless, a practical interpretation of Fig. 4 can be as follows: a decrease in angular speed for constant V and uniform α would in fact increase the tip speed ratio. Therefore, for a scenario where a torque is applied to an autogyro at a slow enough rate to be considered quasi-static, the analysis suggests that the angular speed would move along a trend analogous to the 100 ft/s trend shown in Fig. 7.

3 Catenary Tether Model

To explore the equilibria of a tethered autogyro, one must not only analyze the aerodynamics of the rotor but also the forces of the tether. From the aerodynamic model of Sec. 2.1, the equilibrium thrust T, rotor spinning speed Ω and angle of incidence α of a prospective autogyro are calculated based on given operating conditions. A two-dimensional analysis of the static forces due to the tether is next presented. When combined with the aerodynamics, this will complete the equilibrium analysis of the tethered autogyro in a wind field. In this regard, the tether is modeled as a catenary to provide an adequate approximation of the tether profile and forces.

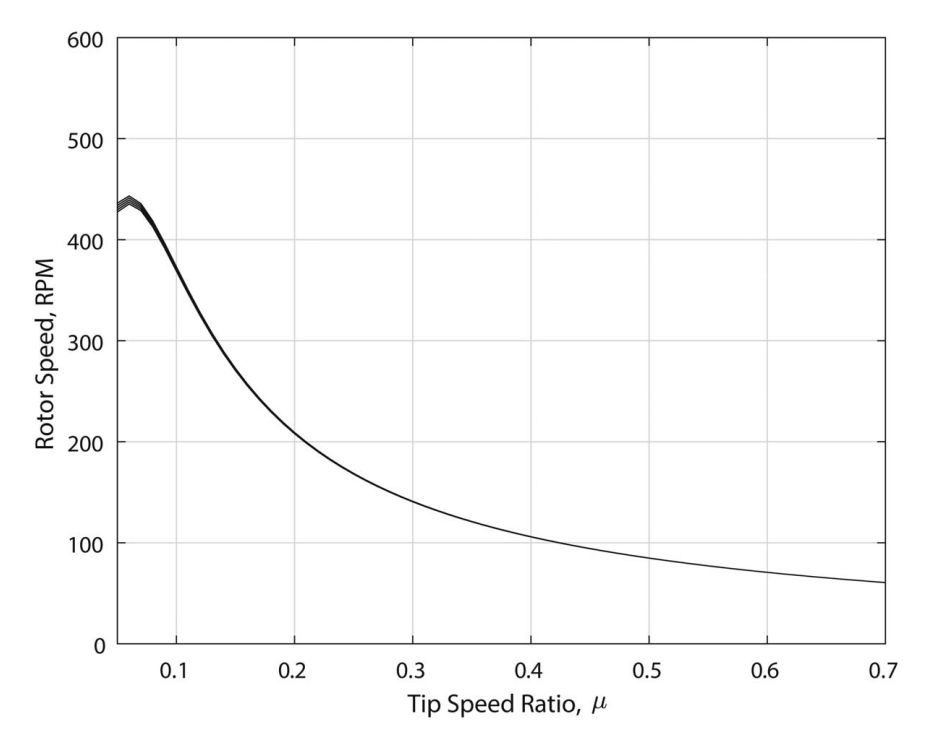


Fig. 7 Angular velocity for various rotor torque inputs. Note: Input torques are same as shown in Fig. 6(a), but trends are almost overlapping and hence indiscernible.

A description of the catenary and its statics analysis can be found in Ref. [40]. Under this approximation, the tether profile can be expressed in a functional form as follows:

$$y = \zeta \left[\cosh \left(\frac{x - q}{\zeta} \right) - \cosh \left(\frac{q}{\zeta} \right) \right]$$
 (18)

where q and ζ are constant parameters of the catenary. A diagram of the catenary tether and forces to be considered for equilibrium analysis are presented in Fig. 8. To solve for the shape of the catenary, a force balance is performed at two different points of reference. Equation (19) represents the x and y-direction force balance of the whole system in Fig. 8, and Eq. (20) represents force balance only on the autogyro (inset in Fig. 8).

$$T\cos\alpha = F_0\sin\eta_0 + H\sin\alpha + m_ag + m_tg$$

$$T\sin\alpha = F_0\cos\eta_0 - H\cos\alpha - F_{t,d}$$
(19)

$$T\cos\alpha = F_1\cos\eta_1 + H\sin\alpha + m_a g$$

$$T\sin\alpha = F_1\sin\eta_1 - H\cos\alpha$$
(20)

where the variables used in Eqs. (19) and (20) are defined in the Nomenclature. For the following analysis, it is assumed that $F_{t,d}$

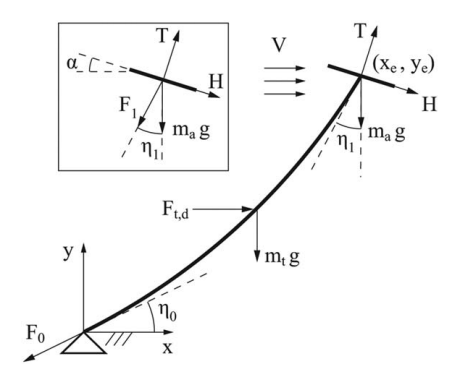


Fig. 8 Static analysis of tethered autogyro

and H provide a negligible effect on the equilibrium behavior and thus are ignored. Equations (19) and (20) can be manipulated to find the angles η_0 and η_1 , as presented in Eqs. (21) and (22).

$$\tan \eta_0 = \frac{T \cos \alpha - (m_a + m_t)g}{T \sin \alpha}$$
 (21)

$$\tan \eta_1 = \frac{T \sin \alpha}{T \cos \alpha - m_a g} \tag{22}$$

Note that the values of T and α are obtained from solving for equilibrium conditions of the autogyro. The two angles η_0 and η_1 , together with the length of the tether l_t , provide enough information to solve for the catenary parameters ζ and q, and the coordinates (x_e, y_e) of the autogyro are given in Eqs. (23)–(26).

$$\zeta = \frac{l_t}{\tan\left(\frac{\pi}{2} - \eta_1\right) - \tan\eta_0} \tag{23}$$

$$q = \zeta \operatorname{arcsinh}(-\tan \eta_0) \tag{24}$$

$$x_e = \zeta \operatorname{arcsinh} \left[\tan \left(\frac{\pi}{2} - \eta_1 \right) \right] + q$$
 (25)

$$y_e = \zeta \left[\cosh\left(\frac{x_e - q}{\zeta}\right) - \cosh\left(\frac{q}{\zeta}\right) \right]$$
 (26)

It is noted that the assumption of negligible H can be justified based on preliminary calculations suggested by Glauert [21]. The assumption of negligible $F_{t,d}$ is based on the slender tether profile in comparison to the exposed area of the autogyro.

4 Computing Equilibria Under Variable Wind Profile

The aforementioned tether model is valid for finding equilibrium positioning of a tethered autogyro system in a uniform wind velocity field. With this assumption, the aerodynamics of the autogyro and the static equilibrium of the tether can be solved independently.

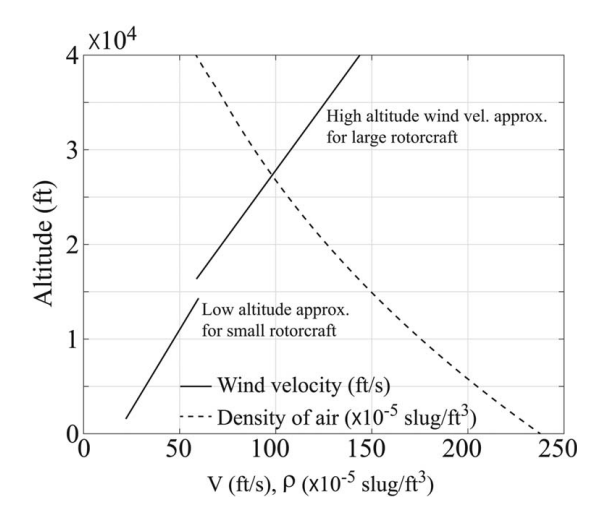


Fig. 9 Wind velocity and air density variation with altitude

However, relaxing this assumption to a more realistic wind field, where V increases linearly as a function of altitude, y, couples the solving of the autogyro aerodynamics and tether profile, as the equilibrium altitude, y_e , solved for by the catenary model may not coincide with the value of V selected as input to the aerodynamic calculations. Instead, it is necessary to implement an iterative method to converge on an altitude where the input V matches the wind speed expected at y_e . It should be noted that for many cases, this equilibrium altitude will not exist, suggesting the given conditions are not suitable for sustainable steady-state tethered autorotation. An equilibrium altitude can be found through the following process:

- (1) Select a value for μ , Q_e , and l_t .
- (2) Initialize V as the velocity at an altitude of l_t .
- (3) Use the above aerodynamic model to solve for T and α .
- (4) Calculate the altitude at x_e using Eqs. (21)–(26).
- (5) Compare the velocity at this altitude, and adjust the guess in the direction of the new velocity.
- (6) Repeat steps 3–5 until the absolute change of V is below a desired threshold (chosen as 10^{-3}), or until the calculated altitude has dropped below a selected minimum threshold suggesting failure.

This process can be significantly expedited by first calculating the aerodynamic results over a sufficiently dense range of μ , Q_e , and V values. Such a data set bypasses the need to resolve the model in step 3. When considering a wide range of altitudes, the role of air density becomes significant and must be considered appropriately. Employing the International Standard Atmosphere model and knowledge of the average wind velocity at a sufficient range of altitudes, the input value of V can be employed to select an appropriate air density for aerodynamic calculations. This improves upon the calculations of Wheatley [25], which assumed a compromise density value analogous to an altitude of approximately 4000 ft.

5 Simulation Results and Favorable Flight Region

Utilizing the aforementioned numerical process, one can explore the feasible equilibrium space for a selected autogyro design and visualize the optimal flight conditions for power generation. The range of equilibria was explored for a wind field with wind velocity and air density varying with altitude. These altitude variations are shown in Fig. 9. Standard atmospheric density variation data are obtained from Ref. [41]. Wind velocity distribution with altitude is based on Refs. [2,42]. Linear velocity distributions were approximated. We present two sets of simulation results. The first concerns high altitudes and a large and heavy autogyro, see Sec. 5.1. In this scenario, we explore regenerative power generation as a feature. The second simulation considers lower altitude deployment and a smaller autogyro, Sec. 5.2. Here we only explore equilibrium autorotation, without power generation. For the two scenarios, the linear wind velocity distributions have slightly different approximations, as shown in Fig. 9.

5.1 Large and Heavy Autogyro at High Altitudes: Potential **Power Generation.** Selected physical parameters for the autogyro and tether used in this simulation are provided in Eq. (17). For blade physical and aerodynamic properties, refer to Sec. 2.2 and the study by Wheatley [25]. The tether is considered to have a weight per unit length of 0.00 lb/ft. This mass density is based on mechanical properties of commercial Kevlar rope found online, for example, Ref. [43]. Specifically, tensile strength was considered and compared against simulation results (presented in Fig. 11). The autogyro weight is chosen at 23.3 slugs, i.e., ≈750 lb. A main component of the weight is anticipated to come from the on-board motor/generator. For the possible power generation determined from simulations (to be discussed using Fig. 11), such motors can weigh as low as \approx 50 lb, [44]. The 750 lb assumption can therefore be considered conservative. The results of tethered autogyro simulation are displayed for a range of μ and Q_e values in Figs. 10 and 11. Figure 10 presents the converged equilibrium altitudes for various tether lengths. The flight conditions that did not allow convergence have been filtered to an altitude value of zero to emphasize the successful equilibrium states. It should be noted that converging states along the border of these successful regions will likely have other undesirable traits such as tether profiles that drop below zero altitude between the base and the autogyro. For optimization purposes, it would be necessary to select a higher threshold altitude to avoid subterranean tether profiles; however, for the purposes of general equilibrium analysis, this filtering was deemed unnecessary. It was observed for the selected autogyro/tether dimensions and weights, see Eq. (17), that successful equilibrium altitude convergence was not achievable for the entire range of μ and Q_e input values for tether lengths below approximately 20,000 ft (≈6 km). From Fig. 10(c), it is evident that higher values of Q_e result in equilibria at lower altitudes for a given tether length. This is expected, since higher Q_e effectively reduces the thrust T. It is also evident that $\mu \approx 0.2$ gives higher equilibrium altitude over the range of feasible Q_e , and hence for a given tether length yields a lower horizontal drift.

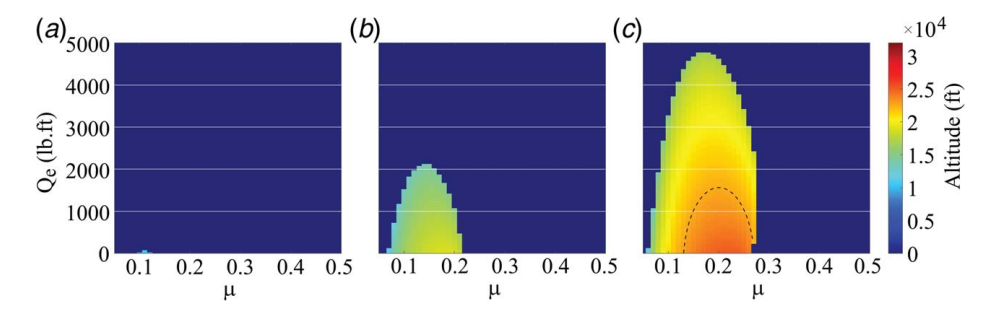


Fig. 10 Equilibrium altitudes for tether lengths: (a) 20,000 ft, (b) 26,000 ft, and (c) 32,000 ft

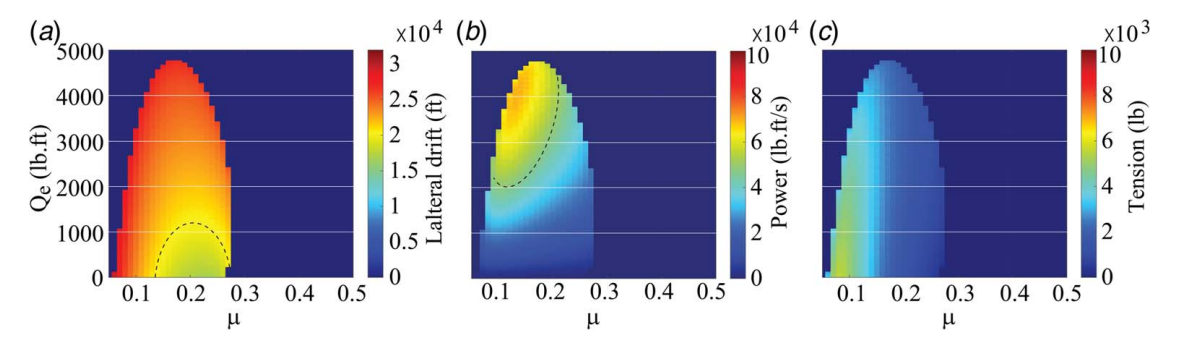


Fig. 11 Equilibria of autogyro specified in Eq. (17) with 32,000 ft tether length: (a) horizontal drift, (b) power, and (c) tension

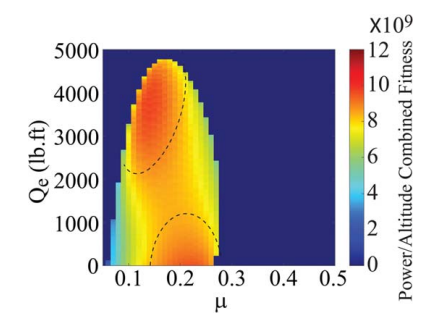


Fig. 12 Comparison of optimal altitude and power regions for 32,000 ft tether

Figures 11(a)-11(c) display the lateral drift of the autogyro from the base, the power generated, and the maximum static tension of the tether, respectively, for a 32,000 ft (approximately 10 km) tether. The lateral drift, power, and tension are important considerations in assessing the characteristics of the equilibria. A high lateral drift may be undesirable as it implies a significant deviation from the launch point. On the other hand, high power is desirable if power generation is the primary goal. We note from the regions enclosed by dashed lines in Figs. 11(a) and 11(b) that these two goals are conflicting. If flying at a higher altitude is desired, then

the equilibria enclosed by the dashed line in Fig. 11(a) is preferred since it equivalently corresponds to high-altitude flight, as shown in Fig. 10(c). Tether tension, Fig. 11(c), is an important practical consideration since it relates to the mechanical integrity of the system. The tether length 32,000 ft was the maximum length considered for this study as the assumption of V varying linearly with y loses justifiablity after this altitude. From Figs. 10(c) and 11(a), it can be seen that the lateral drift of the autogyro has an inverse relationship to that of the equilibrium altitude. This is expected, as a lower flying craft would have more available tether to drift from the base. From Figs. 11(a) and 11(b), we note that generated power is positively correlated with rotor torque Q_e . This is a sensible result, as assuming Ω does not significantly vary, power is directly related to the regenerative braking, Q_e , applied. It is also apparent that power output favors lower values of μ . As μ is defined by an inverse relationship with Ω , it follows that this relation will propagate through to the power output. This inverse relationship between μ and power appears to break down; however, as the autogyro approaches the border of the successful equilibrium space. Given that this region is represented by low altitude flight, it follows that low altitude wind speeds are insufficient for producing the rotational speeds for optimal power output.

Figure 12 plots a combined altitude and power-based fitness for the case of 32,000 ft tether. The fitness function is of the form,

$$J = p_1 y^2 + p_2 (Q_e \Omega)^2$$

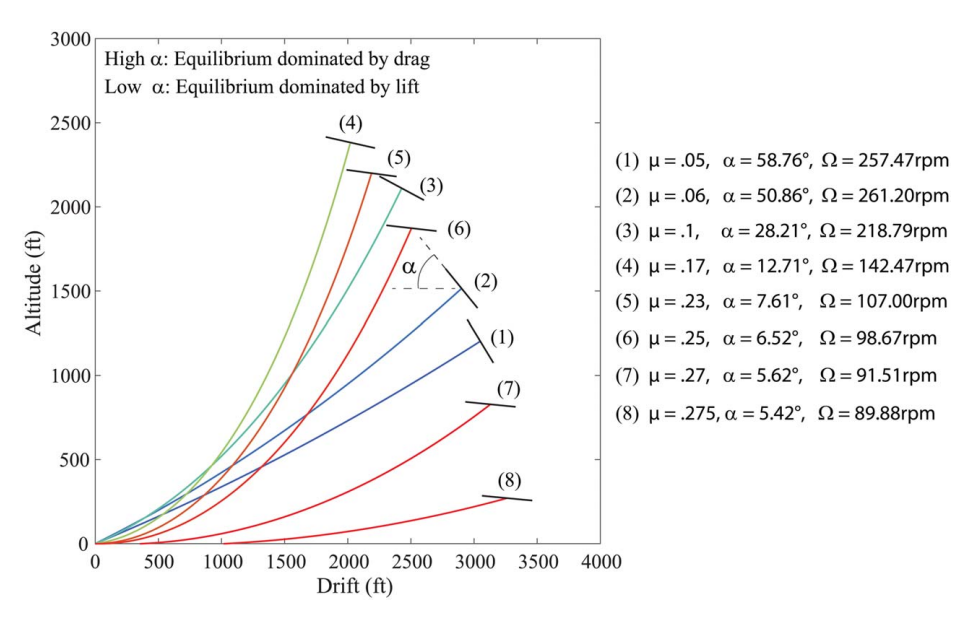


Fig. 13 Tether profile for light autogyro with 1 km (i.e., 3280 ft) tether in uniform 26 ft/s wind field. Tether color scales with the magnitude of μ from blue to red representing low to high μ , respectively.

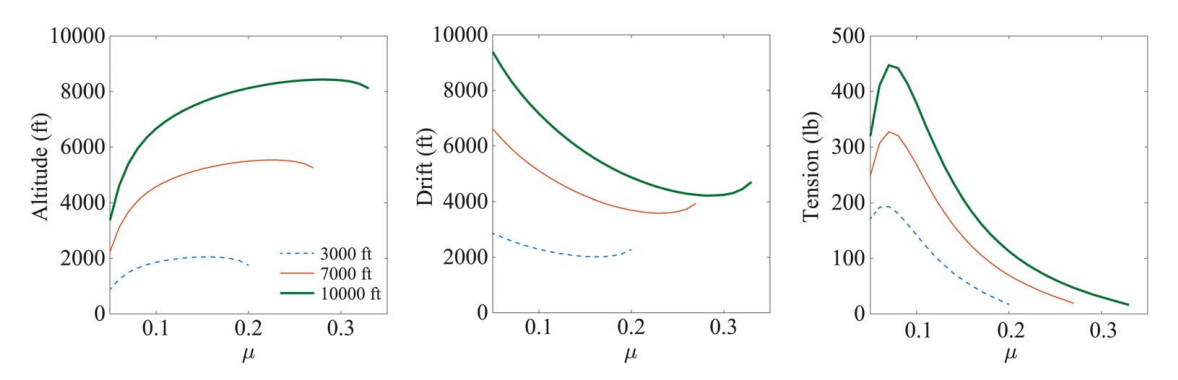


Fig. 14 Equilibria of light autogyro with 3000, 7000, and 10,000 ft tether

where p_1 , $p_2 > 0$ are weighting parameters used to give relative importance to achieving high altitude versus high power. In Fig. 12, we set $p_1/p_2 \approx 200$ to get parity between y and generated power $Q_e \Omega$. Values of J are color coded, and the dark red regions indicate high power generation and/or high-altitude flight. Within the feasible equilibrium space, the dashed lines demarcate the region that yields high-altitude flight (bottom right) and the one that yields high power generation (top left). Comparing with Figs. 10(c) and 11(b), we note that the favorable regions for achieving one or the other are mutually exclusive, indicating high power generation would be achieved at the expense of hovering altitude and vice versa.

5.2 Small, Light Autogyro at Low Altitudes: Hovering Without Power Generation. In this section, we explore the autorotational equilibria of lighter, smaller autogyros at lower altitudes. Here, owing to lesser wind power available at lower altitudes, emphasis is given only on equilibrium hovering conditions and power generation is de-emphasized. Such a setup is deemed suitable for surveillance purposes and for energy efficient flight using autorotation. A lightweight motor, e.g. [45], can be installed on-board to lift the autogyro to the desired altitude range and as a supplement to compensate for variable wind speeds. We consider a autogyro of 35 lb weight and a tether of ≈ 0.005 lb/ft weight per unit length. This leads to a total weight of ≈ 50 lb if a 1 km long tether is used. The blade length R was consider to be 10 ft. The blade chord c was proportionately reduced. The parameters I_1 , M_W , γ , and σ were accordingly scaled.

Figure 13 shows the equilibrium profiles of the system in a 26 ft/s wind field at different angles of incidence α . All simulations were conducted with $Q_e = 0$. We notice that as α reduces, the equilibrium value of μ increases, but the equilibrium altitude reaches a maximum at an intermediate value of μ . This is consistent with the trends observed in Figs. 10(b) and 10(c), where maximum altitude consistently occurred at $\mu \approx 0.2$. From Fig. 13, it is evident that the equilibria at high α , e.g., cases (1) and (2), have a dominant drag force. This causes high drift and taut tether at equilibrium. Lowering α causes the equilibria to be progressively driven by the lift force, e.g., cases (4) and (5), and hence achieve high elevations. Further lowering of α reduces the magnitude of lift force and the resulting equilibria are at low altitudes, e.g., cases (7) and (8). In Fig. 14, we extend the results of the light autogyro to three tether lengths, namely, 3000, 7000, and 10,000 ft and for $Q_e = 0$. The plots, along with the results of Sec. 5.2, confirm that $\mu \approx 0.2$ is an optimal value with respect to maximizing the flying altitude, lowering the horizontal drift and achieving low tether tension.

6 Conclusion and Future Work

This article details a model-based study of the equilibrium characteristics of a tethered autogyro. The aerodynamic model, the tether mechanics, and the proposed numerical method together facilitate the consideration of a wider range of operating conditions

than reported in prior works on modeling autorotation. Specifically, a range of aerodynamic equilibria are obtained as a function of the operating variables, namely, μ , Q_e , and V. It is shown that the results of the presented model accurately match the experimental data of the study by Wheatley [25] when its prescribed wing loading profile is replicated in our model, thereby demonstrating our model's efficacy. The model is simulated to visualize the steady-state behavior of an autogyro and to explore the effects of differing wind velocities and regenerative braking. The aerodynamics is coupled with a static catenary model to approximate the behavior of a tethered autogryo. This coupled model is numerically solved for a wind velocity profile varying with altitude.

The investigation shows the feasibility of performing energy efficient and long duration hovering through autorotation, which can be useful for surveillance of a confined area. In such applications, autorotation could be intermittent or sustained, depending on the consistency of wind speed. In the context of possible power generation, it is observed that sustainable tethered autorotation with simultaneous power generation is likely achievable at significantly high altitudes of a few to several kilometers. Furthermore, it is observed that maximizing the power output for a given autogyro configuration is accompanied by significant drift from the base. It is therefore reasonable to assume that a compromise must be made between the area required by the tethered autogyro mechanism and the power output of the rotor; however, it is possible that an array of smaller autogyros flown at a lower altitude would be able to produce an analogous power output in a more compact space. Testing of this claim would require analysis into the optimal geometric design of a tethered autogyro, which is a topic of future research. The aforementioned analysis is at steady state and thus gives lesser insight into the dynamic behavior of tethered autogyros. Efforts to explore this dynamic behavior and controlling the operating altitude, the drift or the angle of incidence, through active regenerative braking or active tether actuation are currently underway.

Acknowledgment

This work was supported by the National Science Foundation CMMI Grant #1762986, USA.

Conflict of Interest

There are no conflicts of interest.

Data Availability Statement

The datasets generated and supporting the findings of this article are obtainable from the corresponding author upon reasonable request.

Nomenclature

- a =slope of lift curve
- b = number of blades
- c =blade chord
- g = acceleration due to gravity
- v =induced axial velocity
- x = autogyro horizontal position
- y = autogyro altitude
- B =blade radius fraction less tip losses
- K = amplitude of flow variation
- H =longitudinal force
- R =blade radius
- T =thrust force
- V =wind velocity
- $l_t = \text{length of tether}$
- $m_a = \text{mass of autogyro}$
- $m_a = mass of autogyr$
- $m_t = \text{mass of tether}$
- x_e = autogyro horizontal equilibrium position
- y_e = autogyro vertical equilibrium position
- C_T = rotor thrust coefficient
- F_0 = tether tension at base
- F_1 = tether tension at autogyro
- $F_{t,d}$ = total drag force of tether
- I_1 = blade moment of inertia about flapping hinge
- M_W = flapping moment from blade weight
- M_T = flapping moment from thrust
- Q_e = regenerative Braking Torque
- a_0, a_1, b_1, a_2, b_2 = Fourier series parameters of flapping
 - α = angle of incidence
 - β = flapping angle
 - γ = nondimensional mass constant
 - δ = average drag coefficient
 - η_0 = tether angle at base
 - $\eta_1 = \text{tether angle at autogyro}$
 - θ_0 = blade pitch angle at hub
 - θ_1 = blade pitch slope
 - λ = axial flow ratio μ = tip speed ratio
 - $\rho = \text{density of air}$
 - $\rho = \text{density of an}$
 - σ = blade disc solidity
 - ψ = angular position of blade
 - Ω = rotor angular velocity

References

- Fletcher, C. A. J., and Roberts, B. W., 1979, "Electricity Generation From Jet Stream Winds," J. Energy, 3(4), pp. 241–249.
- [2] Durre, I., Vose, R. S., and Wuertz, D. B., 2006, "Overview of the Integrated Global Radiosonde Archive," J. Clim., 19(1), pp. 53–68.
- [3] Roberts, B. W., Shepard, D. H., Caldeira, K., Cannon, M. E., Eccles, D. G., Grenier, A. J., and Freidin, J. F., 2007, "Harnessing High-Altitude Wind Power," IEEE Trans. Energy Convers., 22(1), pp. 136–144.
- [4] Archer, C. L., and Caldeira, K., 2009, "Global Assessment of High-Altitude Wind Power," Energies, 2(2), pp. 307–319.
- [5] Elliott, D., Schwartz, M., Haymes, S., Heimiller, D., Scott, G., Brower, M., Hale, E., and Phelps, B., 2011, "New Wind Energy Resource Potential Estimates for the United States," National Renewable Energy Laboratory, NREL Report No. PR-5500-50439.
- [6] Biscomb, L. I., 1981, "Multiple wind Turbine Tethered Airfoil Wind Energy Conversion System," U.S. Patent No. 4,285,481.
 [7] Biscomb, L. I., 1982, "Tethered Airfoil Wind Energy Conversion System," U.S.
- [7] Biscomb, L. I., 1982, "Tethered Airfoil Wind Energy Conversion System," U.S. Patent No. 4,309,006.
- [8] Pugh, P. F., 1984, "Wind Generator Kite System," U.S. Patent No. 4,486,669.[9] Ockels, W., 2001, "Laddermill, a Novel Concept to Exploit the Energy in the
- [9] Ockels, W., 2001, "Laddermill, a Novel Concept to Exploit the Energy in the Airspace," Aircraft Des., 4(2–3), pp. 81–97.
 [10] Houska, B., and Diehl, M., 2006, "Optimal Control of Towing Kites," IEEE
- [10] Houska, B., and Diehl, M., 2006, "Optimal Control of Towing Kites," IEEE Conference on Decision and Control, San Diego, CA, Dec. 13–15.
- [11] Canale, M., Fagiano, L., Ippolito, M., and Milanese, M., 2006, "Control of Tethered Airfoils for a New Class of Wind Energy Generator," IEEE Conference on Decision and Control, San Diego, CA, Dec. 13–15.
- Conference on Decision and Control, San Diego, CA, Dec. 13–15.

 [12] Lansdorp, B., and Williams, P., 2006, "The Laddermill Innovative Wind Energy From High Altitudes in Holland and Australia," Windpower 2006, Adelaide, Australia, Jan. 1.
- [13] Das, T., Mukherjee, R., Sridhar, R., and Hellum, A., 2011, "Two Dimensional Modeling and Simulation of a Tethered Airfoil System for Harnessing Wind

- Energy," Proceedings of the ASME Dynamic Systems and Control Conference, Arlington, VA. Jan. 1.
- [14] Fechner, U., van der Vlugt, R., Schreuder, E., and Schmehl, R., 2015, "Dynamic Model of a Pumping Kite Power System," Renew. Energy, 83(C), pp. 705–716.
- [15] Riegler, G., Riedler, W., and Horvath, E., 1983, "Transformation of Wind Energy by a High-Altitude Power Plant," J. Energy, 7(1), pp. 92–94.
- [16] Riegler, G., and Riedler, W., 1984, "Tethered Wind Systems for the Generation of Electricity," J. Solar Energy Eng., 106(2), pp. 177–181.
 [17] Vermillion, C., Glass, B., and Rein, A., 2013, "Lighter-Than-Air Wind Energy
- [17] Vermillion, C., Glass, B., and Rein, A., 2013, "Lighter-Than-Air Wind Energy Systems," *Airborne Wind Energy*, U. Ahrens, M. Diehl, and R. Schmehl, eds., Springer, Berlin/Heidelberg, pp. 501–514.
- [18] Das, T., Mukherjee, R., and Cameron, J., 2003, "Optimal Trajectory Planning for Hot-Air Balloons in Linear Wind Fields," AIAA J. Guid. Control Dyn., 26(3), pp. 416–424.
- [19] Charnov, B. H., 2003, From Autogiro to Gyroplane: The Amazing Survival of an Aviation Technology, Praeger Publishers, Westport, CT.
- [20] Leishman, J. G., 2004, "Development of the Autogiro: A Technical Perspective," J. Aircraft, 41(4), pp. 765–781.
- [21] Glauert, H., 1926, "A General Theory of the Autogyro," Presented by the Director of Scientific Research Air Ministry, Reports and Memoranda No. 1111 (Ae. 285).
- [22] Gessow, A., and Myers, G. C., Jr. 1952, Aerodynamics of the Helicopter, Macmillan Company, New York.
- [23] Lock, C. N. H., 1927, "Further Development of Autogyro Theory—Part I," National Advisory Committee for Aeronautics, Reports and Memoranda No. 1127 (Ae. 299).
- [24] Lock, C. N. H., 1927, "Further Development of Autogyro Theory—Part II: A General Treatment of the Flapping Motion," National Advisory Committee for Aeronautics, Reports and Memoranda No. 1127 (Ae. 299).
- [25] Wheatley, J. B., 1934, "An Aerodynamic Analysis of the Autogiro Rotor With a Comparison Between Calculated and Experimental Results," National Advisory Committee for Aeronautics, Report No. 487.
- [26] Gessow, A., and Crim, A. D., 1952, "An Extension of Lifting Rotor Theory to Cover Operations at Large Angles of Attack and High Inflow Conditions," National Advisory Committee for Aeronautics, Technical Note No. 2665.
- [27] Cuerva, A., Sanz-Andres, A., Mesegeur, J., and Espino, J. L., 2006, "An Engineering Modification of the Blade Element Momentum Equation for Vertical Descent: An Autorotation Case Study," J. Am. Helicopter Soc., 51(4), pp. 349–354.
- [28] Wheatley, J. B., 1937, "An Analytical and Experimental Study of the Effect of Periodic Blade Twist on the Thrust, Torque, and Flapping Motion of an Autogiro Rotor," National Advisory Committee for Aeronautics, Technical Note No. 591.
- [29] Houston, S. S., 2002, "Analysis of Rotorcraft Flight Dynamics in Autorotation," J. Guid. Control Dyn., 25(1), pp. 33–39.
- [30] Thomson, D., and Houston, S., 2008, "Advances in the Understanding of Autogyro Flight Dynamics," Ser. AHS Annual Forum, AHS, Montreal, Canada.
- [31] Wheatley, J. B., 1933, "Wing Pressure Distribution and Rotor-Blade Motion of an Autogiro as Determined in Flight," National Advisory Committee for Aeronautics, Technical Note No. 475.
- [32] Floros, M., and Johnson, W., 2007, "Stability and Control Analysis of the Slowed-Rotor Compound Configuration," J. Am. Helicopter Soc., 52(3), pp. 230–253
- [33] Floros, M., and Johnson, W., 2009, "Performance Analysis of the Slowed-Rotor Compound Helicopter Configuration," J. Am. Helicopter Soc., 54(2), p. 22002.
- [34] Rezgui, D., Lowenberg, M., and Bunnies, P., 2008, "A Combined Numerical/ Experimental Continuation Approach Applied to Nonlinear Rotor Dynamics," Progress in Industrial Mathematics at ECMI, vol. 15.
- [35] Rezgui, D. and Lowenberg, M., 2015, "On the Nonlinear Dynamics of a Rotor in Autorotation: A Combined Experimental and Numerical Approach," Philos. Trans. R. Soc. A, 373(2051), p. 23.
- [36] Mackertich, S., and Das, T., 2016, "A Quantitative Energy and Systems Analysis Framework for Airborne Wind Energy Conversion Using Autorotation," American Control Conference, Boston, MA, July 6–8, IEEE, pp. 4996–5001.
- [37] Rimkus, S., Das, T., and Mukherjee, R., 2013, "Stability Analysis of a Tether-Airfoil System," American Control Conference, Washington, DC, June 17–19.
- [38] Salih, B., 2014, "An Introductory Study of the Dynamics of Autorotation for Wind Energy Harvesting," Master's Thesis, University of Central Florida, Orlando, FL.
- [39] Mackertich, S., 2016 "Dynamic Modeling of Autorotation for Simultaneous Lift and Wind Energy Extraction," Master's Thesis, University of Central Florida, Orlando, Fl.
- [40] Beer, F. P., Johnston, E. R., Eisenberg, E. R., and Mazurek, D., 2007, Vector Mechanics for Engineers: Statics, 8th ed., McGraw-Hill, New York.
- [41] "US Standard Atmosphere," 1976, https://www.ngdc.noaa.gov/stp/space-weather/online-publications/miscellaneous/us-standard-atmosphere-1976/us-standard-atmosphere st76-1562 noaa.pdf, Accessed November 23, 2021.
- [42] Archer, C. L., 2013, "An Introduction to Meteorology for Airborne Wind Energy," Airborne Wind Energy, U. Ahrens, M. Diehl, and R. Schmehl, eds., Springer, Berlin/Heidelberg, pp. 81–94.
- [43] "Pelican Rope," https://pelicanrope.com/k-12-kevlar-12-strand-rope/, Accessed November 28, 2021.
- [44] "REB 90 Electric Motor," https://www.mgm-compro.com/electric-motor/80-kw-electric-motor/, Accessed November 28, 2021.
- [45] "RET 20 Electric Motor," https://www.mgm-compro.com/electric-motor/13-kw-electric-motor/, Accessed November 28, 2021.